1st World Congress on Industrial Process Tomography, Buxton, Greater Manchester, April 14-17, 1999.

# Simultaneous Compensation for Attenuation, Scatter and Detector Response for 2D-Emission Tomography on Nuclear Waste with Reduced Data

Raphaël Thierry[1], Jean-Luc Pettier[1], Laurent Desbat[2]
[1]Commissariat à L' Energie Atomique de Cadarache, DCC/DESD/SCCD/LEC
13108 -St-Paul Lez Durance, France,
Phone : (+33) 04-42-25-61-97, (+33) 04-42-25-49-19, Fax : (+33) 04-42-25-73-77,
E-mail : thierry@desdcad.cea.fr, pettier@desdcad.cea.fr
[2]TIMC-IMAG, UMR CNRS 5525
Faculté de medecine, 38706 La Tronche Cedex
Phone : (+33) 04-76-54-96-00, Fax : (+33) 04-76-54-95-55,
E-mail Laurent.Desbat@imag.fr

***Abstract** – We propose a simultaneous correction including three-dimensionnal detector/collimator response, attenuation and diffusion for characterization and appraisal of Nuclear Waste. An Emission Computed Tomography (ECT) imagery was developed in the framework of parallel-hole collimation associated with a HyperPure Germanium (HpGe) detection system. The procedure involves the evaluation of the analytical line spread function (LSF) model with the acquisition of the system LSF by sampling the detection kernel with a multi-energetic europium ($^{152}$Eu) linear source. We use a Maximum a Posteriori (MAP) estimator for the image restitution where the projection processing likelihood is either modeled using a Poissonian or a Gaussian distribution.The introduction of the a priori distribution is chosen as to preserve the image discontinuities by the use of regularization. We compare a MAP-EM One Step Late (OSL) to a deterministic relaxation algorithm for edge-preserving regularization under specific 200-l mock-up and real packages. The analysis of the results showed an improved performance compared to other models, both in quantification and in localization of radio-elements. On the whole experiments it has been showed that volumic model is more precise in term of quantification than global measurements methods even within the latter's assumption framework. Considering the sources repartition, the volumic model globally reduces the blurring and the distortions in heterogeneous activity distributions phantoms. Further experimentions and simulations should give us more information on the influence of parameters, such as the bayesian hyperparameter or the measurement sampling configuration, over the accuracy of the reconstruction.*

**Keywords** : Bayesian Reconstruction, Nonlinear Regularization, LSF Modelling, Nuclear Waste

## 1. INTRODUCTION

Our main objective is the improvement of an emission tomographic method : this expectation is traduced in terms of quantification and localization of multi-energetic radionuclides distributions on Low-Level and Medium-Level (LL & ML) waste packages. In iterative reconstruction methods, these tasks depends strongly on the model accuracy of the maesurement formation process [1]. The necessity of developing a more sophisticated forward modeling is motivated by the ill-conditioned nature inherent to any tomographic phenomenon [2]. The over-all point response is function of multiple degradations factors: attenuation, blurring, scattered photons, noise, collimator septa penetration and intrinsic crystal sensibility. In our work, we can neglect the last phenomenon, because of its relatively poor contribution compared with atttenuation and scattering. Exception made for the computational time process, the most avantageous and accurate approach is to model the spatially varying point spread function (PSF) and treating the reconstruction problem into the resolution of a large system of linearized equations. The litterature reports many reconstruction models where the system PSF was approximated as a two-dimensional function [3-4]. Because of a large parallel hole aperture, the detection kernel can not reasonably be assimilated to a parallel beam. Thus, a non-negligeable part of the photons detected originate from the out-of-slice image pixels and generate a biais by adding themselves to the measurements [5]. Improving

the quantitative precision calls then for a three-dimensional (3-D) model. Moreover, a 3-D modelling will render the reconstruction less sensible to the blurring effects caused by photon crosswalk beyond the transaxial slice [6]. The attenuation correction techniques are as numerous as various. The compensation can be made using filtering methods [7-8], the most common remains the iterative methods [9-10]. The current trend corresponds to the use of an attenuation coefficient map ($\mu$) using a transmission tomograph [11]. In the domain of nuclear waste, the infinite variety of attenuation map distributions do not enable us to use any preliminary map segmentation or pre or post-correcting methods that could speed up a cumbersome iterative method. According to many authors [12], the iterative attenuated projector-backprojector reconstruction algorithms remain one of the more accurate methods, even if time consuming. The correction of the scattered component is compensated through post-processing of the HpGe-spectrum, via the substraction of an assimilated Galton form [13].
Even if we are not confrontated with limited-angle cases, the poor photon quantities emerging from high/medium density packages convey us to work with low resolution aperture and under minimal sampling configurations, at least if we want to cope with reasonable time measurements. In such cases, applying standard full-data reconstruction algorithm, such as filtered backprojection [14], results in poor reconstructions with severe artifacts. Among the many specialized algorithms that have been proposed over the past twenty years, iterative algorithms that incorporate a priori knowledge about the image distribution have displayed the best results. In this paper, we propose to compare the bayesian reconstruction methods, with a gradient-based deterministic approach which is less heavy to implement in terms of time and work required. The aim of this work should lighten us on the contribution and the domain of interest of using a poissonian distribution rather than a classical gaussian model.

## 2. DESCRIPTION OF THE ACQUISITION SYSTEM

The TEMISEC (Tomographe d'EMIssion pour l'Expertise des Colis[1]) facility consists of a mechanical part with a self-motoring support moving the package according to 3 axes ($\theta$ for rotation, Z for elevation and X for the abscissa). The detection includes a HyperPure Germanium detector of 4.7 cm in diameter placed in a cylindrical lead shield and with a parallel-hole lead collimator. We note by $l_{col}, h_{col}$ and $L_{col}$ the collimator-hole dimensions respectively in sidth, height and length. Experiments were performed with a 3-cm open square and 38.5-cm long. The voxels height *h*, will be taken as equal to the exit height of the collimated beam (c.f. Figure 1).
The package dimensions correspond to 200-liter waste drums, i.e. a cylinder of 28.5-cm radius, noted $R_{obj}$ and 85-cm high.
The object attenuation map is obtained either by :

1. a tomodensimetric cross section obtained using a transmission tomograph with a $^{60}$Co irradiant source,
2. using the CARACO mixtures method [15], from a global measurement and a reduced Hubbell database [16],
3. using the Klein-Nishina équations [17] and an average density, in the Compton domain for the interpolation in energy of global or local linear attenuations.

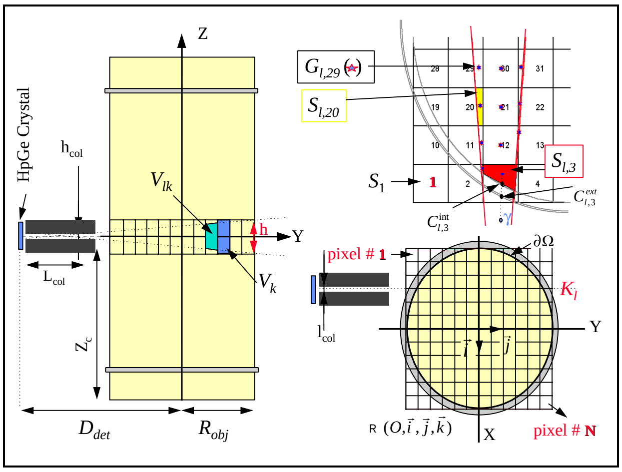

**Figure 1 View according to X and Z axes of the acquisition device and illustration of the quantities $V_k$, $V_{lk}$, $S_k$, $S_{lk}$ and $K_l$**

## 3. PRESENTATION OF THE MODEL

The image, referenced by the volume activity **f**, is reconstructed in a finite $N=n^2$ vectorial space. $\Omega$ representes the object domain, and $\partial\Omega=\left\{(x,y)/x^2+y^2=R_{obj}^2\right\}$ its compass. For any point M, we have

$$\mathbf{f}(M)=\sum_{i,j=1}^{n} f_{ij}\phi_{ij}(M)=\sum_{k=1}^{n^2} f_k\phi_k(M) \tag{1}$$

where the space of base functions $f_{ij}$ are the kronecker operator corresponding to a classic cartesian discretization. Yet, for the following paragraph, we will use the second form, a more alleviated image-vectorial representation. We note R $(O,\vec{i},\vec{j},\vec{k})$ the fixed reference object where $(O,\vec{k})$ is the system rotating axis, axially

---

[1] Emission Tomograph for Waste Appraisal

positionned at the height $Z_c$ of the examination (c.f Figure 1).

We note ***m*** the measurement vector, of size $\mathbf{M} = \mathbf{n}_\theta . \mathbf{n}_d$ , where $\mathbf{n}_\theta$ is the number of angular positions equally spaced around 360° and $\mathbf{n}_d$ the number of measurements performed by projection.

The compensation of attenuation, diffusion and of detector response is calculated via the projection matrix $\mathbf{H} \overset{def}{=} \left( \mathrm{H}_{l,k} \right)_{l=1\ldots M, k=1\ldots N}$, where the element $\mathrm{H}_{l,k}$ expresses the proportion (probability) of voxel *k* to influence on the measurement *l*. The classically *M*-by-*N* matricial formulation obtained is

$$\mathrm{H}\,\mathbf{f} = m \tag{2}$$

In all the paragraphs below, we will name $m$ the linear attenuation function (cm$^{-1}$), and occasionnally we make mention of $m_{cont}$ the container linear attenuation. The attenuation energy dependency is not explicitly expressed, nevertheless we shall remember that for each equation, one must read $m(E)$ *and* $m_{cont}$(E) instead of $m$ *and* $m_{cont}$.

## 4. SCATTER COMPENSATION

The problem of the Compton diffusion has mostly been treated according to four large families [18]: that working with spectral windows, that which attempts to model the phenomenon in the projection/retroprojection operator, those based on a weighting of the detected events, those attempting to eliminate the scattered through deconvolution methods, through spectral analysis or by using a secondary energy window. The evaluation of the scatter response is based on the assimilation of the Compton continuum to a Galton form. The contributing value $N_{scat}(E_i)$ in the energy canal $E_i \in \left[E_1, E_2\right]$ is given by :

$$N_{scat}(E_i) = N\left(E_1\right) + \left(N\left(E_2\right) - N\left(E_1\right)\right) \frac{\sum_{E_j=E_1}^{E_i} N(E_j)}{\sum_{E_j=E_1}^{E_2} N(E_j)} \tag{3}$$

*N(E$_i$)* is the total photon-counts at energy canal *E$_i$*, the numerator and denominator respectively represents the partial sum (until E) and total sum in the energy window selected*.* The elimination of the scattering componant is achieved finally by adding the values $N_{scat}(E_i)$ obtained.

The accuracy of the method is greatly guaranteed by the high energy resolution of the HyperPure Germanium crystal (0.66% at 140 keV). The detector specificity has been used many times to quantify the Compton diffusion fraction in the Anger cameras [19] and has been validated by Monte-Carlo algorithms [20] .

## 5. COMPENSATION OF ATTENUATION AND DETECTOR RESPONSE

We note $M_{\det}$ the detector-central point and $l \in \left[1..M\right]$, the index refering to the measurement. The theorical[2] volume detection kernel, noted *K$_l$*, is a square based pyramid with vertex $M_{\det} + .5 L_{col} \vec{j}$ .

Let *V$_k$* be the volume related to the voxel *k,* and *S$_k$* the surface corresponding to the voxel-base on the cross section plane. We note *V$_{lk}$* the intersection of *K$_l$* with *V$_k$*, as well as *S$_{lk}$*, intersection of *K$_l$* and *S$_k$*. (c.f. Figure 1). For each measurement, the projection operator of our system is given by :

$$\begin{aligned} m_l &= \iiint_{K_l} f(M).PSF(M)\,dM \\ &= \iiint_{K_l} f(M).R_{\det}^{p}(M).\exp\left( -\int_{M_{\det}}^{M} \mu(l)\,dl \right) dM \end{aligned} \tag{4}$$

The second equality of (4) expresses the decomposition of the PSF as the product of $R_{\det}^{p}(M)$ the spatial response of the system, by the objet attenuation factor. By decomposing *K$_l$* on $\Gamma_l = \left\{ k \in \left[1..N\right] / V_{lk} = K_l \cap V_k \neq 0 \right\}$, the set of voxels having non-nil intersection with the detection space, then equation (4) becomes :

$$\begin{aligned} m_l &= \sum_{k \in \Gamma_l} \iiint_{V_{lk}} f(M) PSF(M) dM \\ &= \sum_{k \in \Gamma_l} \iint_{S_{lk}} \left\{ \int_{\left[-h/2, h/2\right]} f(x,y,z) PSF(x,y,z) dz \right\} dxdy \end{aligned} \tag{5}$$

The LSF is obtained by integrating the PSF over z :

$$LSF(x,y) = \int_{-h/2}^{h/2} R_{\det}^{p}(M).\exp\left( -\int_{M_{\det}}^{M} \mu(l)\,dl \right) dz \tag{6}$$

We now admit a first assumption [a$_0$] : the attenuation factor is independent of variable z. At this time we can re-write (6) as follows :

---

[2] when septa penetration is negligeable

$$LSF(x,y) \approx \exp\left( - \int_{M_{\det}}^{(x,y,0)} \mu(l)dl \right) \int_{-\frac{h}{2}}^{\frac{h}{2}} R_{\det}^{p}(M)dz \qquad (7)$$

[a$_0$] was verified in the framework of homogeneous attenuations and for axially constant distributions. In both cases, we can show that for any $\mu \in [0{,}0.3]$ and any $(x,y) \in \Omega$, (7) is a good numerical approximation of (6) [21].

The attenuation evaluation distinguishes itself whenever the attenuation map is given from transmission tomography or supposed constant. In the first case, we determine the integral calculation by a nearest neighbor interpolation or bilinear interpolation along the line connecting the point *M* and $C_{lk}^{ext}$ and the raw and columns of the grid. In absence of tomodensimetric data, we determine $C_{lk}^{\text{int}}$ and $C_{lk}^{ext}$ (c.f. Figure 1), the intersections linking *M<sub>det</sub>* to *M* with the inside edge, respectively the ouside edge of the drum. The calculation of the attenuation can be simplified to obtain the following expression :

$$\exp\left( - \int_{M_{\det}}^{M} \mu(l)dl \right) = e^{-\mu_{cont} \cdot \left\| C_{lk}^{ext} C_{lk}^{\text{int}} \right\| - \mu_{obj} \cdot \left\| MC_{lk}^{\text{int}} \right\|} \qquad (8)$$

We have chosen an homogeneous volumic distribution of activity , so for any $V_k$ we set :

$$\forall (x,y,z) \in V_k, \quad f(x,y,z) = f_k \qquad (9)$$

and we propose two different way of approaching the surfacic integral calculation. The first method decomposes the polygon $S_{lk}$ in $(n_{lk} - 2)$ triangles, where $n_{lk}$ are the vertices of $S_{lk}$, $(3 \le n_{lk} \le 6)$[3]. This routine allows a rapid and exact extraction of the surface of $S_{lk}$ and its barycentric coordinates $G_{lk}\left(x_{lk}^{G}, y_{lk}^{G}, 0\right)$. We evaluate the integral calculation using the barycentre value, and using approximation (7), thus

$$\begin{aligned} m_l &\approx \sum_{k \in \Gamma_l} f_k \cdot \iint_{S_{lk}} LSF(G_{lk})\, dxdy \\ &= \sum_{k \in \Gamma_l} f_k . e^{-\int_{M_{\det}}^{G_{lk}} \mu(l)dl} . S_{lk} \cdot \int_{-\frac{h}{2}}^{\frac{h}{2}} R_{\det}^{p}(x_{lk}^{g}, y_{lk}^{g}, z)dz \end{aligned} \qquad (10)$$

Identifying (10) and (2) the matrix element $\mathrm{H}_{lk}$ is

$$\mathrm{H}_{lk} = S_{lk} . e^{-\int_{M_{\det}}^{G_{lk}} \mu(l)dl} . \int_{-\frac{h}{2}}^{\frac{h}{2}} R_{\det}^{p}(x_{lk}^{g}, y_{lk}^{g}, z)dz \qquad (11)$$

The calculation accuracy of $\mathrm{H}_{lk}$ depends on the voxels size and on the LSF behavior on $S_{lk}$. To supply for the partial volume effect [22], we propose to increase the calculation points on $S_{lk}$, with a over-sampled second grid of finite elements, including $N' = \tau^2 N$ voxels, where *t* is an integer strictly greater than 1.

We respectively define the set of voxel indexes $\Lambda_k(\tau) = \left\{ k' \in \left[1..\tau^2 N\right] / V_k = \bigcup_{k'} V_{k'} \right\}$ making by their union the voxel *k*, and $\Lambda_{lk}(\tau) = \left\{ k' \in \left[1..\tau^2 N\right] / (x_{k'}^{g}, y_{k'}^{g}) \in S_{lk} \right\}$ the points sub-set of $\Lambda_k(\tau)$ which centers $(x_{k'}^{g}, y_{k'}^{g})$ are contained in $S_{lk}$. With a sufficiently fine grid-subdivision, the second grid-voxels retained in $\Lambda_{lk}(\tau)$ form a good approximation of the initial volume calculation $S_{lk}$ :

$$\lim_{\tau \to +\infty} \bigcup_{k' \in \Lambda_{lk}(\tau)} S_{k'} = S_{lk} \qquad (12)$$

Thus, under the previous condition, (10) becomes :

$$\begin{aligned} m_l &= \sum_{k \in \Gamma_l} f_k \cdot \sum_{k' \in \Lambda_{lk}(\tau)} \iint_{S_{k'}} LSF(x,y)dxdy \\ &\approx \sum_{k \in \Gamma_l} f_k \cdot \sum_{k' \in \Lambda_{lk}(\tau)} LSF(x_{k'}^{g}, y_{k'}^{g}).S_{k'} \end{aligned} \qquad (13)$$

Finally, a finest evaluation of element $\mathrm{H}_{lk}$ is :

$$\mathrm{H}_{lk} = \sum_{k' \in \Lambda_{lk}(\tau)} S_{k'} . e^{-\int_{M_{\det}}^{G_{lk}} \mu(l)dl} \int_{-\frac{h}{2}}^{\frac{h}{2}} R_{\det}^{p}(x_{k'}^{g}, y_{k'}^{g}, z)dz$$

(14)

The spatial response expression of the collimated detector is given from the solid angle seen from point M(x,y,z), so :

$$\begin{aligned} R_{\det}^{p}(M) &= \frac{1}{4\pi} \iint_{S_M} \frac{d\vec{M}.d\vec{S}}{\left\| MS \right\|^2} \\ &= \frac{1}{4\pi} \iint_{S_M} \frac{\cos\chi . dudw}{(u-x)^2 + (D_{\det} + y)^2 + (w-z)^2} \end{aligned} \qquad (15)$$

---

[3] The vertices coordinates are obtained through the intersection of $S_k$ with the object outline $\partial\Omega$ and the kernel $K_l$.

$S_M$ is the domain of surface $l_m.h_m$ belonging to the detection plane observable from point *M*, (Figure 2) $d\vec{S}$ is the normal unit vector on the detector plane, $d\vec{M}$ is the unit vector of the line connecting M to S, cos$\chi$ is the angle formed between $d\vec{S}$ and $d\vec{M}$

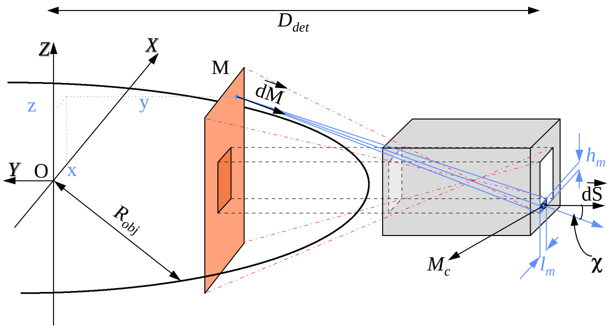

**Figure 2 : Solid angle generated by point M**

We show in [21] that according to the great distance between the source space Ω and the detection plane, and the relatively small angle aperture, we can reasonably consider that $\cos\chi \approx 1$. Besides, the distance $\|MS\|$ only slightly varies when S covers $S_M$ and can be optimaly approached by that taken at the central point S=$M_c(x_c,-D_{det},z_c)$ of the rectangle $S_M$ . At this moment, the resulting approximation of (15) can be expressed by :

$$R^{p}_{\det}(M) \approx \frac{l_m(M).h_m(M)}{4\pi.\left\|MM_c\right\|^2} \tag{16}$$

This last expression is particular as its integration according to *z* leads to a literal expression [21] :
The figure below illutrate the corresponding PSF on the domain object and the LSF for a non attenuating object :

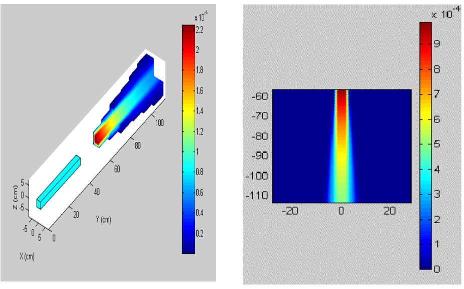

**Figure 3 : Theoretical PSF and LSF (right) according to equation (16).**

## 6. PSF AND LSF EXPERIMENTAL VALIDATIONS

The validation of equation (16) required the use of 241-Americium ($^{241}$Am) and $^{152}$Eu point sources in order to cover a large energy domain, and validated on height pre-selected energy peaks [4]. The source was successively placed at a minimum distance, $y_{\min} = D_{\det} - R_{obj}$, in the center $y_{moy} = D_{\det}$, and at maximum distance $y_{\max} = D_{\det} + R_{obj}$. A scale factor was needed to readjust the theoretical data to those from the experiment. This factor was chosen so as to realize the Minimum Mean Square Error (MMSE) between experimental and theoretical data. All of them indicate a good prediction of the phenomenon and the quadratic residual errors range from 0 to 28%. The maximum error being reached at the maximum energy peak (Figure 3-bottom) at $y_{\min}$ where the septa penetration effect is the major cause for the blurring beyond the theoretical detection kernel. On the top, the $^{241}$Am-source placed at $y_{\min}$ results in a excellent adequation, (septas penetration is nearly insignificant at 59 keV)

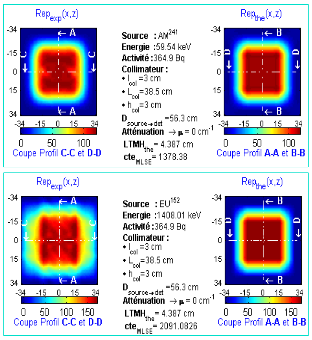

**Figure 4 : Experimental and theoretical PSF on $^{241}$Am (top) and $^{152}$Eu (bottom)**

The $^{152}$Eu linear source used for the LSF validation is.8-cm diameter, 73-cm long. It was successively positionned on $32^2$ points, sampling the detection kernel. The essential aim is to characterize calibration through numerical interpolation which must be applied in order to obtain a quantitative coherence between modelling and measurements.
The calibration $c(y,E)$ was taken as a degree 3- polynome of both variables, interpolating the datas $c(y_i,E_j)$ achieving the minimum error between the experimental LSF(.,$y_i$ ) profile obtained at energy $E_j$ and the theoretical LSF.

---

[4] 59 keV for $^{241}$Am and 121 keV, 244 keV, 344 keV, 779 keV, 964 keV, 1112 keV, 1408 keV for $^{152}$Eu

# 7. RECONSTRUCTION METHODS

## 7.1. Poissonian likelihood

The MAP estimation in the context of Bayesian approach is attractive because it enables the incorporation of a large class of *a priori* image distribution, and ensure better convergence and stability properties [23]. The Baye's formula states that :

$$\Pr(\mathbf{f}\,|\,\mathbf{m}) = \frac{\Pr(\mathbf{m}|\mathbf{f})\Pr(\mathbf{f})}{\Pr(\mathbf{m})} \qquad (17)$$

$\Pr(\mathbf{f}\,|\,\mathbf{m})$ representes the *a posteriori* distribution, $\Pr(\mathbf{m}|\mathbf{f})$ the likelihood, $\Pr(\mathbf{f})$ and $\Pr(\mathbf{m})$ are respectively the image and measure prior distribution. If we consider the image distribution as constant, the MAP estimator and the Maximum Likelihood Estimator (MLE), noted $\mathbf{f}_{ML}$, realizing the maximum of $\Pr(\mathbf{m}|\mathbf{f})$, are identical. The expectation maximisation (EM) iterative algorithm [24] is classically used to compute $\mathbf{f}_{ML}$ : The explicit iterative scheme is : For any $\mathbf{f}^0 \geq 0$,

$$\forall k,\ f_k^{p+1} = \frac{f_k^p}{\sum_l \mathrm{H}_{lk}} \sum_l m_l \frac{\mathrm{H}_{lk}}{\sum_m \mathrm{H}_{l,m} f_m^p} \qquad (18)$$

Yet, the ill-posedness of ML-reconstruction [25] is numerically traduced by an undesirable tendency to amplify artefacts at higher iteration numbers. Moreover the ML-EM slow convergence rate is a supplying reason to turn toward MAP-based algorithm. Since it is hard to infer global properties to the image, most common approaches involves assumptions on the local spatial properties accounting to Gibbs distributions[5]. A general Gibbs distribution form is :

$$\Pr(\mathbf{f}) = \frac{1}{Z}\exp\left(-\beta E_P(\mathbf{f})\right) \qquad (19)$$

where the parameter β controls the weight of the *a priori*, Z is a normalizing constant, and $E_P(\mathbf{f})$ represents the system energy function [26]. Its form depends on the MRFs neighborhood order and on the choice of a potential function, noted φ. In our case, we use a second order MRF, constituted by height neighbours, and we limit the dependency at two adjacents pixels cliques. For a simplified 1st order MRF, the expression of the system energy is

$$E_P(\mathbf{f}) = \sum_{i,j} \varphi\left(\left(D_x^\delta f\right)_{i,j}\right) + \sum_{i,j} \varphi\left(\left(D_y^\delta f\right)_{i,j}\right) \qquad (20a)$$

where

$$(D_x^\delta f)_{ij} \overset{def}{=} \frac{f_{ij} - f_{ij-1}}{\delta},\ (D_y^\delta f)_{ij} \overset{def}{=} \frac{f_{ij} - f_{i-1j}}{\delta} \qquad (20b)$$

are the horizontal and vertical gradient operator. The second parameter δ acts like a scaling factor on the gradient of the image. The associated MAP estimator optimise the functionnal cost:

$$\mathbf{f}_{MAP} = \max_{\mathbf{f}\geq 0} E_{tot}(\mathbf{f})$$

$$= \max_{\mathbf{f}\geq 0}\left\{\sum_l m_l \log\Big(\sum_k \mathrm{H}_{l,k} f_k\Big) - \sum_k \mathrm{H}_{l,k} f_k - \beta E_P(\mathbf{f})\right\}$$

(21)

We uses a One-Step-Late (OSL) scheme [28]. To nullify the non-linear normal equations of (21), Green proposed to evaluate the partial derivative of the a priori energy with the last iterate $\mathbf{f}^p$ instead of the current estimate $\mathbf{f}^{p+1}$. This latter can then explicitely be given according to $\mathbf{f}^p$ by the formula

$$f_k^{p+1} = \frac{f_k^p}{\sum_l \mathrm{H}_{l,k} + \beta \left.\dfrac{\partial E_P(\mathbf{f})}{\partial f_k}\right|_{f_k^p}} \sum_l m_l \frac{\mathrm{H}_{l,k}}{\sum_m \mathrm{H}_{l,m} f_m^p} \qquad (22)$$

So at each iteration the MAP-EM-OSL increases the MAP (log-) probability; nevertheless we must be carefull with the choice of the potential function since it can render the whole MAP-functional non-convex and thus converge to only local optimum. Besides, the choice of the couple $(\beta,\delta)$ is delicate since it affects directly the image characteritics. We choose Green's potential $\varphi(x) = 2\log[\cosh(x)]$, because of his convexity and its numerical characteristics respecting the (edge-preserving) conditions [29]:

$$\lim_{u\to 0^+} \varphi'(u)/2u = 1, \qquad (23\text{-i})$$

$$\lim_{u\to +\infty} \varphi'(u)/2u = 0 \qquad (23\text{-ii})$$

and $\varphi'(u)/2u$ continuous and strictly decreasing on [0,+∞[. (23-iii)

The function $\varphi'(u)/2u$ plays an important role, since it intervenes directly in the regularization as a weighted-laplacian filter on the pixels of the image.

## 7.2. Gaussian likelihood

Using a gaussian distribution the associated MAP estimator is expressed by :

$$\mathbf{f}_{MAP} = \min_{\mathbf{f}\geq 0} E_{tot}(\mathbf{f}) = \min_{\mathbf{f}\geq 0}\left\{\|m - H\mathbf{f}\|^2 + \beta E_P(\mathbf{f})\right\} \qquad (24)$$

---

[5] that are closely linked to Markov Random Fields (MRF).

The optimization of (24) uses the concept developed by [30]. This recently proposed algorithm transforms the original non-linear, and possibly nonconvex system, into a sequence of quadratic optimization problems. The implementation uses the additive ARTUR algorithm [31], which development is briefly exposed below :

The half-quadratic regularization introduces auxiliairy variables *b*, and it has been shown that under specific conditions, i.e. $\varphi$ verifying clauses (23) [32], we have :

$$\varphi(u) = \inf_{0 \le b \le 1} \left( bu^2 + \psi(b) \right) \tag{25}$$

where $\psi$ is a strictly convex and continuous function. Substituting (25) in the cost function $E_{tot}(\mathbf{f})$, it becomes equivalent to minimize the dual energy $E^*_{tot}(b,\mathbf{f})$ which is now at *b* fixed, quadratic with respect to **f**. The problem is greatly simplified accouting to the fact that for a fixed value **f**, *b(u)* solution of (25) is precisely the weighted function, i.e. [32]

$$b(u) = \inf_{0 \le b \le 1} \left( bu^2 + \psi(b) \right) = \frac{\varphi'(u)}{2u} \tag{25}$$

The resolution of the initial non-linear problem is now transformed into an alternative minimisation of **b** and **f**. The general algorithm[6] is :Given $f^0$, Repeat

$$\left| \begin{array}{l} b_k^{n+1} = \left( \left. \dfrac{\varphi'(D_x^\delta f^n)}{2(D_x^\delta f^n)} \right|_k , \left. \dfrac{\varphi'(D_y^\delta f^n)}{2(D_y^\delta f^n)} \right|_k \right) \\ \left( H^t H + \dfrac{\beta}{\delta^2} \Delta_{pond}^{n+1} \right) f^{n+1} = H^t m \end{array} \right. \tag{26}$$

Until convergence

where $\Delta_{pond}^{n+1}$ represents the weighted laplacian obtained through the solving of the normal equations of (24). The linear system, since $\Delta_{pond}^{n+1}$ depends on the updated and un-updated values of f, is solved with a successive over relaxation (SOR) algorithm [33].

# 8. EXPERIMENTAL VALIDATION

## 8.1. Quantitative results on 200-l phantoms

The mock-up is constituted with a linear source positioning system, configurable in matrix. It has been evaluated on four activity configurations : 1 source in the center (the most heretogeneous case) until seven helicoidaly disposed sources (the most heretogeneous case). The matrix was successively homogeneously filled with air, polyethylen ( average density of 0.54 ± 0.04) and sand (average density of 1.46 ± 0.11). The $^{152}$Eu sources average activity was of 10 Mbq on the 03/04/96. Each experiment is associated with the undimensional variable $\mu R_{obj}$, traducing the average number of mean free path value, noted $\lambda$ $(\lambda = \mu^{-1})$.

**Figure 5 : The four sources configurations used (the 120°-oriented three big spots are aluminium maintaining rods)**

We compare the results with a classical "Ray-Driven" modeling [34] and a global measurement and correction method called MARCO-CARACO [16] which assumes a physical homogeneous repartition. This last method corresponds to the «Rockwell approximation» [35], and is only valid if the package is sufficiently far from the detector. We present on the Y-axis the activity ratio between the global reconstructed activity and the known real activity, the whole function of $\mu R_o$ (c.f. Figure 4 ).

For the less homogeneous configurations (1 and 3 sources) until the most homogeneous case (5 and 7-sources), the tomographic reconstruction shows an improvement on quantitative accurary over a global measurement method. ECT provides excellent results until $\mu R_o$=4. MEPHISTO[7] shows a better behavior when reaching this limit over the central ray approximation (ray-driven). Over this limit, unsufficient photon counting combined with the unprecision on the lineic attenuation in the photoelectric attenuation domain deteriorate the precision on quantification and localisation.

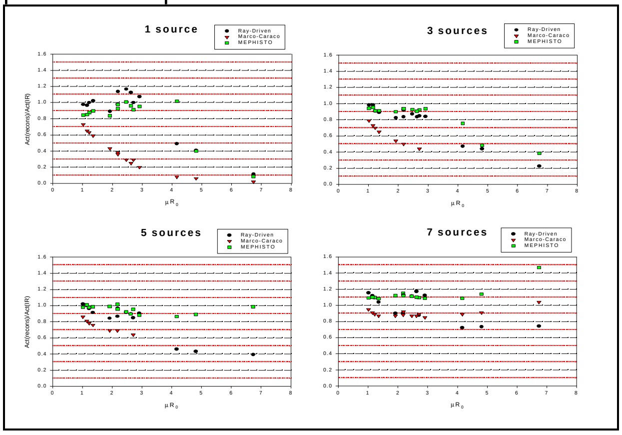

**Figure 6 : Comparison of recontructed Activity ratio**

For the 5 and 7-sources configurations, emission tomography and more particularely MEPHISTO enables an optimal quantification until the upper limit of our experiments, which is $\mu R_o$=7. A slightly deterioration is yet discernible at the highest attenuation which is due to the primordial

---

[6] for a first order neighborhood

[7] Multi-Energetic PHoton Imagery through Segmented Tomography is the named given to the volumic algorithm

influence of the object-peripheral source . When passing at the nearest source-to-detector distance, the large volume of the voxel including the source induces a partial volume effect. The magnitude of this effect varies with the non-stationnary and anisotropic spatial resolution. Thus, since the gradient of the response is maximum at short distance and the fact that the activity repartition in the mock-up is more likely to follow a Dirac than a evenly voxel spreading, the model inherent to MEPHISTO generates a bias in this case. In the ray-driven as well, a bi-linear interpolation through coarse grid automatically leads to errors.

### 8.2. Image reconstruction

Before analysing the algorithms behavior, we fisrt propose an illustration that underlines the influence of an heterogeneous attenuation map correction over a global approximation : the reconstruction was realized for the 1-source configuration, at 121 keV, in the sand-matrix, i.e corresponding to $\mu R_o=7$.

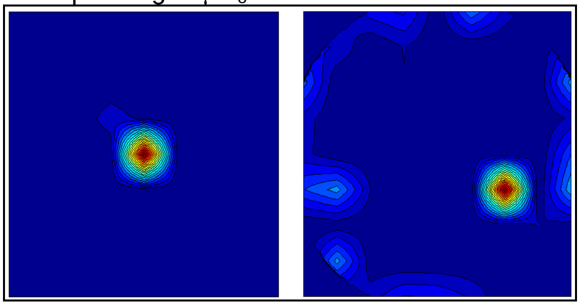

**Figure 7 : ML reconstruction with a heterogeneous μ-map (left), with a constant μ determined by Klein-Nishina (right).**

The nature of the benefit introduced by the consideration of the attenuation response, is clear from Figure 7, where the source positioning is respected and periferal artifacts are considerably diminished.

The following intercomparaison was made on the 7-source configuration, at 1408 keV, in the polyethylen-matrix, i.e corresponding to $\mu R_o=1.15$.

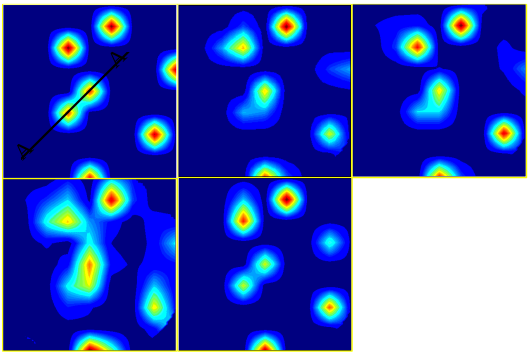

**Figure 8 : Image reconstructions with different algorithms**

We performed the four reconstructions on 200 iterations, and the parameters settings for ARTUR and the MAP-EM-OSL were $\beta$=1.5167e-9 $\delta$=2.5e5. We also use a Tikhonov regularization derivated from the ARTUR scheme by using a quadratic potential function ($\varphi(u)=u^2$). Since this potential does not respect the condition (23), it enables to better perceive the improvement brought by a anisotropic regularization, i.e. when compared to ARTUR. The regularization parameter was set at the same value as $\beta$. On figure 8, from left to the right, from the top to the bottom :

The reel phantome image, a ML-EM reconstruction and the ARTUR reconstruction. Below, the Tikhonov regularization resolved with a Conjuguate Gradient (CG) method [33], and the MAP-EM-OSL.

On Figure 9 features the evolution of the Normalized Mean Square Error (NMSE) between the real image $\hat{\mathbf{f}}$ and the differents estimations, i.e. $\mathbf{NMSE}(n)=\left\|\hat{\mathbf{f}}-\mathbf{f}^n\right\|/\left\|\mathbf{f}^n\right\|$, function of the iterations.

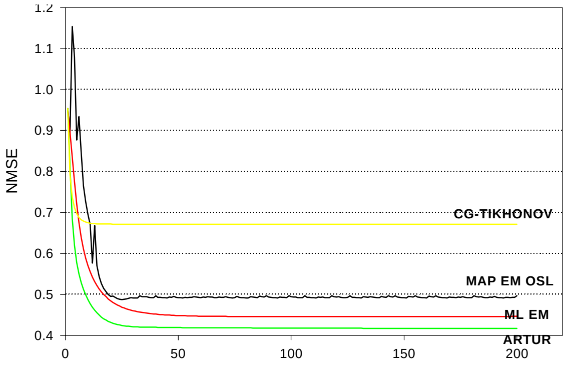

**Figure 9 : NMSE versus iterations**

On figure 10, we represent the relative norm between two succesive iterations of each algorithm.

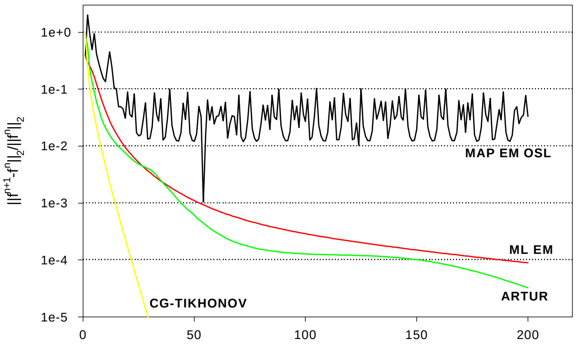

**Figure 10 : Relative Residual Norm versus iterations**

On Figure 11, the profil of the reconstructed image and the real phantom along the segment A-A (figure 8)

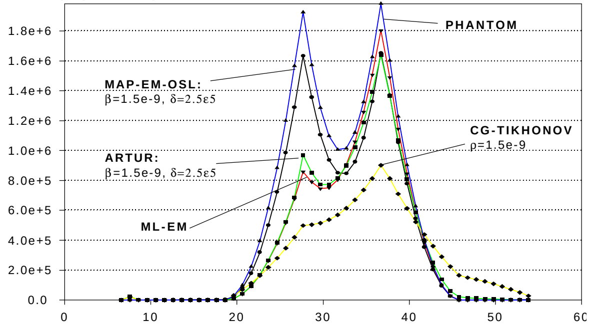

**Figure 11 : Profil intercomparaison along the segment A-A**

In terms of visual aspects, i.e Figure 8 and 10, the MAP-EM-OSL is the only one that clearly distinguish 7 sources. Yet according to Figure 9, ARTUR shows the best convergence rate and reaches a minimal NMSE after only 30 iterations. Indeed, the fact that MAP-EM-OSL commits an error placement on the upper-right periferal source prevent any further NMSE reducing.

## 9. CONCLUSION

In this paper, MEPHISTO, a unified two-dimensional reconstruction method for simultaneous compensation of attenuation, scatter, and three-dimensional analytical geometric response has been presented. The method was evaluated on multienergetic sources of $^{152}$Eu, for three different density matrix and compared with a central ray approximation and a global measurement method. The results confirmed that an exact correction of attenuation (by coupling of transmission tomographic maps) indeniably improve the localisation and shape of hot spots. Moreover, on the whole panel of configurations, the volumic model showed to improve quantification of the global radionuclides activity. Delicate configurations, such as the combination of high density matrix and radionuclides emmiting in the Compton domain seriously impoverish the statitics of the measurements and induce incertainities over the atttenuation that affect the modeling. We propose to overcome the difficulty within the image reconstruction framework by introducing *a priori* information on the image distribution modeled on a markovian field. The results showed that the bayesian methods can lead to better results in term of shape recognition and localisation of activity heterogeneities. Nevertheless, some problems require further studies, such as the optimal selection of the hyperparameters contained in the bayesian model, or questions regarding the particular form of the gibbs distribution employed, and the computational expense associated with their implementation.

## REFERENCES

[1] G.L. Zeng and G.T. Gullberg "Three-dimensional iterative reconstruction algorithms with attenuation and geometric point response correction." IEEE Trans. Nucl. sci. 38(2):693-702,1991

[2] M.E. Davison, "The ill-conditionned nature of the limited angle tomography problem," SIAM J. Appl. Math.,vol. 43, pp. 428-448, 1983

[3] A. Formiconi , A. Pupi , A. Passeri. "Compensation of spatial system response in SPECT with conjuguate gradient reconstruction technique," Phys. Med. Biol. 34:69-84,1989

[4] B.M.W. Tsui, ,H. Hu,D.R. Gilland and G.T. Gullberg, "Implementation of simultaneous attenuation and detector response correction in SPECT," IEEE Trans Nucl. Sci. 35 : 778-783, 1988

[5] M.T.Munley, C.E. Floyd,J.E. Bowsher,G.D. Tourassi, and R.E. Coleman, "Out of plane photons in SPECT," IEEE Trans. Nucl. Sci., vol 38, pp. 776-779, 1991

[6] F.J. Beekman, C. Kamphuis, and M.A. Viergever, "Improved SPECT quantitation using fully three-dimentional iterative spatially variant scatter response compensation," IEEE Trans. Med. Imag, vol. 15, no. 4, August 1996.

[7] G. Gullberg and T. Budinger, "The use of filtering methods to compensate for constant attenuation in single photon emission computed tomography," Internat.J. of Imag. Syst. and Technol. 28(2):142-157,1989

[8] L. Chang. "A method for attenuation correction in radionucleide computed tomography." IEEE Trans. Nucl. Sci. 25 (1):638-639,1978

[9] G Gullberg, G Zeng, B.M.W Tsui and J. Hagius J "An iterative reconstruction algorithm for single photon emission computed tomography with cone-beam geometry." Internat. Syst. and technol.,1:169-186,1989

[10] A Maze. "Iterative reconstruction methods for nonuniform attenuation distribution in SPECT." J. of Nucl. Med. 34 (7),1993

[11] M.H Bourguignon,et al. "Correction of attenuation in SPECT with an attenuation coefficient map: a new method." J. Nucl.Biol. Med 37:26-32,1993

[12] B.M.W. Tsui *et al*, "Correction of Nonunform attenuation in Cardiac SPECT imaging," J. Nucl. Med. 30:497-507,1989

[13] Morel J, Lepy M.C. "Traitement de l'information en spectrometrie gamma ou X". C.E.A Saclay LMRI 1986

[14] F. Natterer . "The mathematics of computerized tomography" Ed. Wiley 1989

[15] B. Chabalier, "Non Destructive Determination of Activity," Nuclear Technology Vol. 115 Aug. 1996

[16] N. Huot,B Chabalier,P. Bonifay, "Effets des hétérogénéités radioactives sur les mesures d'activité par la méthode MARCO-CARACO" Note technique C.E.A DCC/DESD/SCCD. Mars 1996

[17] REF KLEIN NISHINA

[18] I. Buvat, H. Benali, A Todd-Pokropek, R. Di Paola, "Scatter correction in scintigraphy : the state of art," Eur. J Nucl Med 21:675-694, 1994

[19] M. Singh and C. Horne, "Use of a Germanium Detector to Optimize Scatter Correction in SPECT," J. Nucl. Med. 28(2):1853-1860, dec 1987

[20] K.R. Zasadny, K.F. Koral, C.E. Floyd and R.J. Jaszczak, "Measurement of Compton scattering in phantoms by germanium detector," IEEE Trans. Nucl. Sci, 37(2)642-646,1990

[21] R Thierry, J.L. Pettier "Modélisation volumique pour la caractérisation de colis de déchets par tomographie d'émission gamma". Note technique (à paraitre) C.E.A DCC/DESD/SCCD. Decembre 1998

[22] P.H. Pretorius *et al*, "Reducing the influence of partial volume effect on SPECT activity quantification with 3D modelling of spatial resolution in iterative reconstruction," Phys. Med. Biol. 43, pp. 407-420,1998.

[23] K. Lange, "Convergence of EM Image reconstruction algorithms with Gibbs smoothing," IEEE Trans. Med. Imag., vol 9, No 4, pp. 439-446, dec 1990

[24] Shepp L.A Vardi Y " Maximum likelihood Reconstruction for Emission Tomography." IEEE Trans. Med. Imag.vol MI-1, No 2, pp 113-121, Oct 1982

[25] R.A. Tapia and J.R Thompson, "Nonparametric probability density estimation," Baltimore, MD John Hopkins University, 1978.

[26] Geman S. and Geman D. "Stochastic Relaxation, Gibbs Distributions, and the Bayesian restoration of images." IEEE Trans. Pattren Anal. Machine Intell. Vol PAMI-6, pp721-741, Nov 1984.

[27] T.J Hebert and S.S Gopal, "The GEM MAP algorithm with 3-D SPECT system response," IEEE Trans. Med. Imag.Vol 11, No 1, pp 81-90, March 1992

[28] P.J Green "Bayesian reconstruction from emission tomgraphy data using a modified EM algorithm" IEEE Trans. Med. Imag, Vol MI-9, N°1, pp. 84-93, March 1990

[29] P. Charbonnier, "Reconstruction d'image : régularisation avec prise en compte des discontinuités." PhD thesis, Univ. Nice, Sophia-Antipolis, France, Sept 1994.

[30] D. Geman and C. Yang, " Nonlinear image recovery with half-quadratic regularization anf FFTs," preprint, March 1993

[31] G Aubert, M. Barlaud, P Mathieu and P. Charbonnier, "ARTUR, an adaptative deterministic relaxation algorithm for Edge-preserving tomographic reconstruction", Tech Rep 93-76, 13S, Univ. Nice-Sophia-Antipolis, 1993.

[32] G Aubert, M. Barlaud, P Mathieu and P. Charbonnier, "Theorems for Edge-preserving regularization in Computed Imaging", Research Report N° 94-01, 13S, Univ. Nice-Sophia-Antipolis, 1994.

[33] P Lascaux, M Theodor, "Analyse matricielle appliquée à l'art de l'ingenieur." Ed Masson, 1986

[34] Joseph P.M. "An improved Algorithm for reprojection rays through pixel images." IEEE Transactions on Medical Imaging, vol MI-1, no 3, November 1982

[35] Rockwell T. " Reactor Shielding Design Manual", U.S. Atomic Energy Commission Mc Graw Hill Book Company, Inc. 1956